Spatially distributed MIMO sonar systems: principles and capabilities

Spatially distributed MIMO sonar systems: principles and capabilities

Yan Pailhas, Yvan Petillot, *Member, IEEE*, Keith Brown, Bernard Mulgrew, *Fellow, IEEE*

Abstract

Multiple Input Multiple Output sonar systems offer new perspectives for target detection and area surveillance. This paper introduces a unified formulation for sonar MIMO systems and focuses on the target detection and recognition capability of these systems. The multiplication of the number of transmitters and receivers not only provides a greater variety in terms of target view angles but also provides meaningful statistics on the target itself. Assuming that views are independent and the MIMO system is large enough, we demonstrate that target recognition is possible with only one MIMO snapshot. By studying the detection performance of MIMO sonars we also demonstrate that such systems solve the speckle noise and decorrelate individual scatterers inside one cell resolution, leading to super-resolution imaging. We also show that, if carefully designed, MIMO systems can surpass the resolution of a SAS (Synthetic Aperture Sonar) system using the same bandwidth. All the discussed properties are derived from the independent view assumption. Fulfilling this assumption drives the design and efficiency of such systems.

Index Terms

MIMO sonar systems, multi-static sonars, target recognition, super-resolution sonar images.

I. Introduction

MIMO stands for Multiple Input Multiple Output. As stated in [1], MIMO does not have a strict and formal definition. In this paper, we define MIMO as a structure with multiple transmitters and receivers which transmits a variety of waveforms and has the capability to

Y. Pailhas, Y. Petillot and K. Brown are with the Ocean Systems Laboratory, Heriot Watt University, Edinburgh, UK. email: Y.Pailhas@hw.ac.uk. B. Mulgrew is with the School of Engineering at Edinburgh University.

jointly process all the received signals. MIMO systems can have collocated [2] or widely separated [3] antennas. This paper focuses on spatially distributed MIMO structures. MIMO has been widely investigated during the last two decades for wireless communications, and have received a lot of interest in recent years in the radar community [4]–[8]. Radar researchers have pointed out multiple advantages of these systems such as diversity gain for target detection [2], [6], [9], [10], angle of arrival [11], [12] and Doppler estimation [3], [13]. Coherent processing also allows improved resolution for target localisation [14].

Multistatic sonar systems have also been investigated, mainly in the anti-submarine warfare community. Such systems surpass monostatic sonar systems in target localisation [15] and detection performance [16]. The CMRE (Centre for Maritime Research and Experimentation), in particular, has developed a deployable low frequency multi-static sonar system called DEMUS. The DEMUS hardware consists of one source and three receiver buoys and can be denominated as a SIMO (Single Input Multiple Output) system. A series of trials including preDEMUS06 and SEABAR07 [17], [18] have been conducted by CMRE. Results of these trials show better detection and tracking performances [17]–[22]. Very few studies however have investigated full MIMO sonar systems.

This paper focuses on the detection and recognition problems using MIMO sonar systems with widely separated antennas. The main contributions of the paper are:

1) the reformulation of the MIMO equations for sonar systems (section II). The model proposed is based on the target form function formulation and, unlike the radar formulation, intelligibly dissociates propagation from target response. Although the model is derived from the radar formulation, this approach emphasises the fundamental differences between radar and sonar systems.
2) a new bistatic modelling of cylindrical shell using virtual point scatterers (section III). The echo of man-made objects with a relatively simple shape can be modelled with very few scattering points. We show in section III an example of this statement.
3) the derivation of the recognition capability of MIMO sonar systems (section IV-A). Studying the target response from a MIMO system leads to the observation that, with enough independent observations, the target probability density function is very well estimated with a single snapshot. An example of automatic target recognition is

presented.

4) the proof that MIMO systems can resolve the speckle (section IV-B). By fusing the target response of a well designed MIMO system, we demonstrate that when the number of independent observations is close to infinity, all the scatterers within one resolution cell decorrelate.

It is important to note that the results 3) and 4) on the MIMO sonar capabilities are derived independently of any particular MIMO system geometry. The assumption of independent observations between all the MIMO pairs is discussed (section IV-C). A novel measure of inter-correlation for a MIMO sonar system based on the distance correlation [23] is proposed to measure effectively the degree of independence of all the MIMO observations.

This paper is organised as follow: In section II we present the radar MIMO formulation and derive the broadband sonar MIMO expression; section II-A focuses on the MIMO response of targets modelled by a finite point scatterers model and in section III a finite point scatterer model for a bistatic system is presented for a resonant target. Finally in section IV we demonstrate the sonar MIMO capabilities in terms of target recognition and MIMO very high resolution imaging.

II. Reformulation of the broadband MIMO sonar problem

A. The RADAR formulation

The first formulation for MIMO systems for target detection has been made by the radar community [4]. The MIMO system model can usually be expressed by: $\overline{\mathbf{r}} = \overline{\overline{\mathbf{H}}}.\overline{\mathbf{s}} + \overline{\mathbf{n}}$, where $\overline{\mathbf{r}}$ represents the receivers, $\overline{\mathbf{s}}$ the transmitters, $\overline{\mathbf{n}}$ the noise, and $\overline{\overline{\mathbf{H}}}$ the channel matrix. The channel matrix includes the wave propagation in the medium from any transmitter to any receiver and the target reflections. Some models use the point target assumption [24] while more advanced versions use rectangular-shape targets composed of an infinite number of scatterers [6]. We present here the most popular model for a radar target which is the finite scatterer model [3], [10].

In [3] the authors formulate the narrowband MIMO radar equation using a finite point target model. A target is represented here with Q scattering points spatially distributed. Let $\{X_q\}_{q\in[1,Q]}$ be their locations. The reflectivity of each scattering point is represented by

the complex random variable ζ_q. All the ζ_q are assumed to be zero-mean, independent and identically distributed with a variance $\mathbb{E}[|\zeta_q|^2] = 1/Q$. Let Σ be the reflectivity matrix of the target, $\Sigma = \mathrm{diag}(\zeta_1, ..., \zeta_Q)$. By using this notation the average RCS (radar cross section) of the target $\{X_q\}$, $\mathbb{E}[\Sigma\Sigma^T]$, is normalised to 1.

The MIMO system comprises a set of K transmitters and L receivers. Each transmitter k sends the pulse $\sqrt{E/K}.s_k(t)$ where E is the total transmit energy of the MIMO system. We assume that all the pulses $s_k(t)$ are normalised. With these notations, the signal $z_{lk}(t)$ from transmitter t to receiver l and interacting with the target can be written as:

$$z_{lk}(t) = \sqrt{\frac{E}{K}} \sum_{q=1}^{Q} h_{lk}^{(q)} s_k \left(t - \tau_{tk}(X_q) - \tau_{rl}(X_q)\right) \tag{1}$$

$$\text{with} \quad h_{lk}^{(q)} = \zeta_q \mathrm{e}^{-j2\pi f_c[\tau_{tk}(X_q)+\tau_{rl}(X_q)]} \tag{2}$$

where f_c is carrier frequency, $\tau_{tk}(X_q)$ represents the propagation time delay between the transmitter k and the scattering point X_q, $\tau_{rl}(X_q)$ represents the propagation time delay between the scattering point X_q and the receiver l. Note that $h_{lk}^{(q)}$ represents the total phase shift due to the propagation from the transmitter k to the scattering point X_q, the propagation from the scattering point X_q to the receiver l and the reflection on the scattering point X_q.

Assuming the Q scattering points are close together (*i.e.* within a resolution cell), we can write:

$$\begin{aligned} s_k \left(t - \tau_{tk}(X_q) - \tau_{rl}(X_q)\right) &\approx s_k \left(t - \tau_{tk}(X_0) - \tau_{rl}(X_0)\right) \\ &= s_k^l(t, X_0) \end{aligned} \tag{3}$$

where X_0 is the centre of gravity of the target $\{X_q\}$. So Eq.. (1) becomes:

$$z_{lk}(t) = \sqrt{\frac{E}{K}} s_k^l(t, X_0) \left(\sum_{q=1}^{Q} \zeta_q \mathrm{e}^{-j2\pi f_c[\tau_{tk}(X_q)+\tau_{rl}(X_q)]} \right) \quad (4)$$

$$= \sqrt{\frac{E}{K}} \left(\sum_{q=1}^{Q} h_{lk}^{(q)} \right) s_k^l(t, X_0) \quad (5)$$

$$= \sqrt{\frac{E}{K}}\ h_{lk}\ s_k^l(t, X_0) \quad (6)$$

using the notation $h_{lk} = \sum_{q=1}^{Q} h_{lk}^{(q)}$. Assuming a multi-targets scenario including N_0 targets, the total signal $r_{lk}(t)$ from transmitter l to receiver k can be written as:

$$r_{lk}(t) = \sum_{n=1}^{N_0} z_{lk}^{(n)}(t) + n_{lk}(t) \quad (7)$$

where n_{lk} is the total noise at receiver k. Note that the interaction between targets is ignored here.

In this section we propose a reformulation of the Haimovich model presented in section II-A to suit broadband sonar systems. Because the target response, the seabed and surface response or even the wave propagation is strongly dependent of the frequency, a broadband sonar formulation is more appropriate in the Fourier domain [25]–[27]. It also allows a clear separation of the different mechanisms involved in the echo formation. Eq. (1) becomes:

$$Z_{lk}(\omega) = \sqrt{\frac{E}{K}} \sum_{q=1}^{Q} h_{lk}^{(q)} S_k(\omega) \mathrm{e}^{-j\omega[\tau_{tk}(X_q)+\tau_{rl}(X_q)]} \quad (8)$$

Using the following notations:

$$\begin{aligned} \tau_{tk}(X_q) &= \tau_{tk}(X_0) + \tilde{\tau}_{tk}(X_q) \\ \tau_{rl}(X_q) &= \tau_{rl}(X_0) + \tilde{\tau}_{tk}(X_q) \end{aligned} \quad (9)$$

and

$$H_{lk}(X_0, \omega) = \sqrt{\frac{E}{K}} . \mathrm{e}^{-j(2\pi f_c+\omega).[\tau_{tk}(X_0)+\tau_{rl}(X_0)]} \quad (10)$$

the following expression can be derived:

$$\begin{aligned} Z_{lk}(\omega) &= H_{lk}(X_0,\omega)\left(\sum_{q=1}^{Q}\tilde{h}_{lk}^{(q)}\mathbf{e}^{-j\omega[\tilde{\tau}_{tk}(X_q)+\tilde{\tau}_{rl}(X_q)]}\right)S_k(\omega) \\ &= H_{lk}(X_0,\omega)F_\infty(\omega,\theta_l,\phi_k)S_k(\omega) \end{aligned} \tag{11}$$

where θ_l is the angle of view of the target from the transmitter and ϕ_k is the angle of view of the target from the receiver. Eq. (11) can be interpreted as follows: the first term corresponds to the propagation of the wave to and from the target, the second term is the form function of the target, the third term is the transmitted signal.

The main advantage of this formulation is the clear separation between propagation terms and target reflection terms. In our formulation the target form function F_∞ is independent of any particular model. The second advantage of this formulation is that the generalization of Eq. (11) including multipath and attenuation terms is straightforward. Considering P multipaths between the transmitter l and the receiver k Eq. (11) becomes:

$$Z_{lk}(\omega) = \sum_{p=1}^{P} A^{(p)}(\omega)H_{lk}^{(p)}(X_0,\omega)F_\infty(\omega,\theta_l^{(p)},\phi_k^{(p)})S_k(\omega) \tag{12}$$

$A^{(p)}(\omega)$ is the attenuation through path p.

In this formulation we choose to ignore the Doppler shift introduced by a moving target. Considering a target moving at $v = 1\text{m.s}^{-1}$ and a pulse with f_0 = 50kHz central frequency, the maximum Doppler shift is $\delta f = 2f_0v/c \approx 67$Hz. Narrow band Doppler sensitive pulses have minimal spectral width. In that case the spectral width is dominated by the pulse width. With a pulse duration of $\tau = 10^{-3}$s, the maximal Doppler shift of 67Hz is then marginal compared to the 2.5kHz spectral width.

III. Virtual point scatterers model for a cylindrical shell

We derived earlier the MIMO sonar model from the finite point scatterer model. In this section, we analyse further this target model. Despite the simplicity of this model we demonstrated in [28]–[30] that for monostatic sonar systems, man-made objects can be reasonably well modelled using this approach. We even showed in [30] that this assumption leads to interesting features to distinguish man-made objects from natural objects. We extend

here the monostatic point scatterer model to an accurate bistatic model for a low impedance shell cylinder.

In [29], we demonstrated that the sound scattering of a low impedance shell cylinder is analogous to the reflection by two spherical mirrors (one convex for the front face and one concave for the back face) in geometrical optics. Fig. 1 shows the echo formation of an acoustic wave reflected by a plastic cylindrical shell. The location of the two echo centres $\mathbf{A1}$ and $\mathbf{A2}$ (in Fig. 1) can be computed thanks to the well known formula of reflection by a spherical mirror [31]:

$$\frac{1}{\overline{\mathbf{SA}'}} + \frac{1}{\overline{\mathbf{SA}}} = \frac{2}{\overline{\mathbf{SC}}} \tag{13}$$

where $\mathbf{A}$ and $\mathbf{A}'$ represent respectively the source and the source image, $\mathbf{C}$ the centre of the sphere and $\mathbf{SC}$ the radius of the sphere.

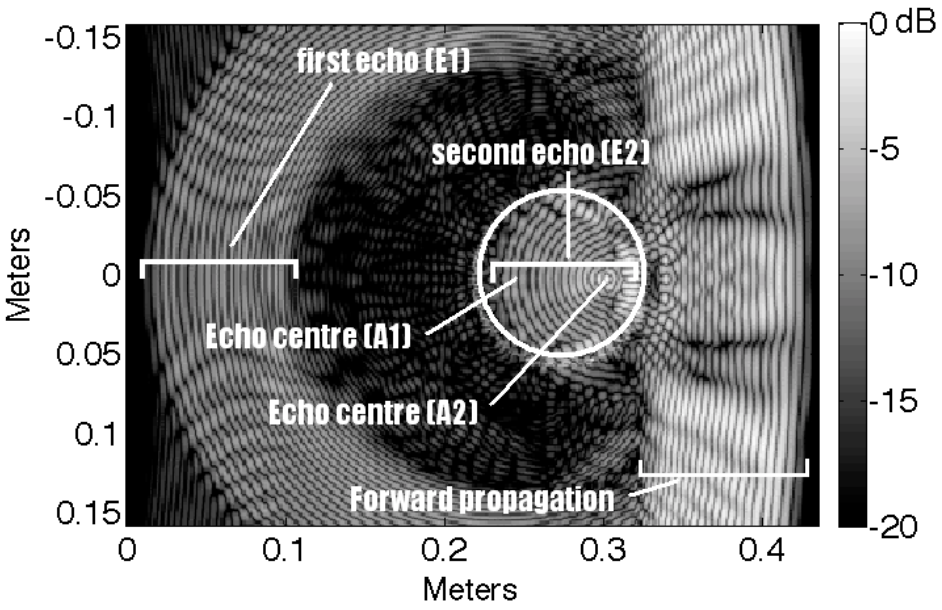

Fig. 1. Sound interaction between a plane wave and a plastic cylindrical shell.

$\mathbf{A1}$ and $\mathbf{A2}$ are the source images of an incoming plane wave. The two echo centres, $\mathbf{A1}$ and $\mathbf{A2}$, are then exactly between the centre of the cylinder and the front and the back of the cylinder. In our model $\mathbf{A1}$ and $\mathbf{A2}$ will represent the virtual scatterers. They act like point sources, but contrary to scattering points, they emit the received pulse with a delay (positive

or negative).

The transmitter k transmits the pulse $s_k(t)$. The acoustic wave is reflected by the cylinder modelled by the virtual scatterers **A1** and **A2** to receiver l. Eq. (14) expresses the acoustic field $r_{kl}(t)$ received at receiver l:

$$\begin{aligned} r_{kl}(t) = \quad & s_k\left(t - \tau_{kC} - \tfrac{3}{2}\tfrac{SC}{c} - \tau_{A_1 l}\right) \mathbf{e}^{i\psi_1} + \\ & s_k\left(t - \tau_{kC} + \tfrac{3}{2}\tfrac{SC}{c} - \tau_{A_2 l}\right) \mathbf{e}^{i\psi_2} \end{aligned} \tag{14}$$

where SC represents the radius of the cylinder, c the speed of sound in water, C the centre of the cylinder and the notation τ_{kC} represents the propagation time between the transmitter k and C, $\tau_{A_i l}$ represents the propagation time between the virtual scatterer Ai and the receiver l. ψ_i corresponds to the phase shift introduced by the virtual scatterer Ai. For this case $\psi_1 = \psi_2 = 0$.

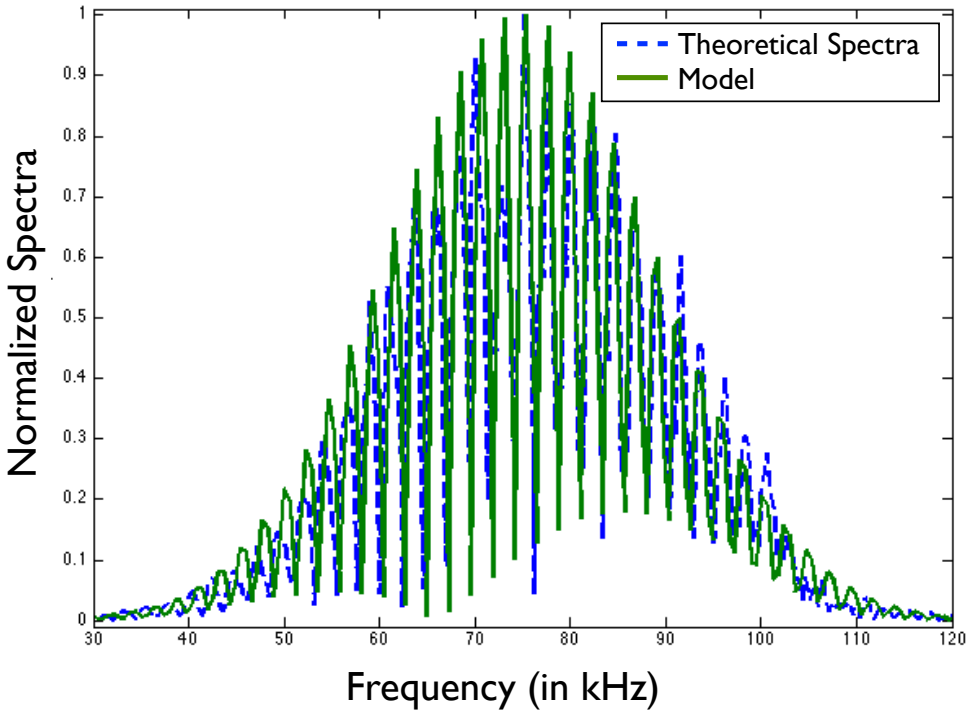

Fig. 2. Matching between the normalized spectra between the theoretical prediction [32] and our model.

The two terms $-\frac{3}{2}\frac{SC}{c}$ and $+\frac{3}{2}\frac{SC}{c}$ represent the negative and positive delays of the virtual scatterers. In Fig. 2 we compare the echo spectra of our virtual scattering point model with the analytic solution given in [32]. In this example, the cylindrical shell is made of PVC,

its diameter is 32 cm and its thickness is 3 mm. The receiver is placed at 4 metres from the shell at an angle of 30° relative to broadside. An excellent match is found between the theoretical prediction and our model.

This result as well as results from [28]–[30] reenforces our assumption that a simple shaped man-made target echo can be modelled with a finite and small number of scatterers. This assumption differs greatly from radar models where target are modelled with high density scattering points.

IV. Statistical MIMO

A. Automatic Target Recognition using statistical MIMO

It is interesting to note that the term $\sum_{q=1}^{Q} h_{lk}^{(q)}$ in Eq. (5) corresponds in essence to a random walk in the complex plane where each step $h_{lk}^{(q)}$ can be modelled by a random variable. Random walks are often used in physics to model the particle diffusion in gas or liquid. Lets assume that the reflectivity coefficients ζ_q can be modelled by the random variable $\frac{1}{\sqrt{Q}}\mathrm{e}^{2i\pi U}$ where $U \in [0,1]$ is the uniform distribution. This hypothesis implies that:

$$h_{lk}^{(q)} \;=\; \frac{1}{\sqrt{Q}}\mathrm{e}^{2i\pi U} \tag{15}$$

The independence of each $h_{lk}^{(q)}$ lies in the fact that the antennas are widely spaced and there is no correlation between each transmit $\rightarrow$ scattering point $\rightarrow$ receiver path. Thanks to the central limit theorem we can compute the limit:

$$\lim_{Q\to+\infty} \sqrt{\left|\sum_{q=1}^{Q} h_{lk}^{(q)}\right|^2} \sim \mathrm{Rayleigh}(1/\sqrt{2}) \tag{16}$$

$\mathrm{Rayleigh}(\sigma)$ represents the Rayleigh distributed random variable with parameter σ. Here $\sigma = 1/\sqrt{2}$. However the central limit theorem gives only the asymptotic behaviour of the random variable. As the number of scattering points becomes large, the reflectivity of the target can be modelled by a Rayleigh distribution.

Eq. (16) links the expected reflectivity of the target $\{X_q\}$ to the expected diffusion of a particle following the random walk $\sum_{q=1}^{Q} h_{lk}^{(q)}$. It has been proven in [33] that the convergence

of Eq. (16) is fast. To demonstrate this we use the Moivre-Laplace representation (which compares probability density functions) to visualize the probability density functions (PDF) convergence. In Fig. 3 we compute the PDF of the reflectivity of a Q scattering points target using the model given by Eq. (15). As this figure shows, for $Q \geq 5$ the reflectivity PDF matches closely the Rayleigh$(1/\sqrt{2})$ probability distribution. In Fig. 3 we can see that the probability function of the 100 scatterer target and Rayleigh$(1/\sqrt{2})$ are almost indistinguishable.

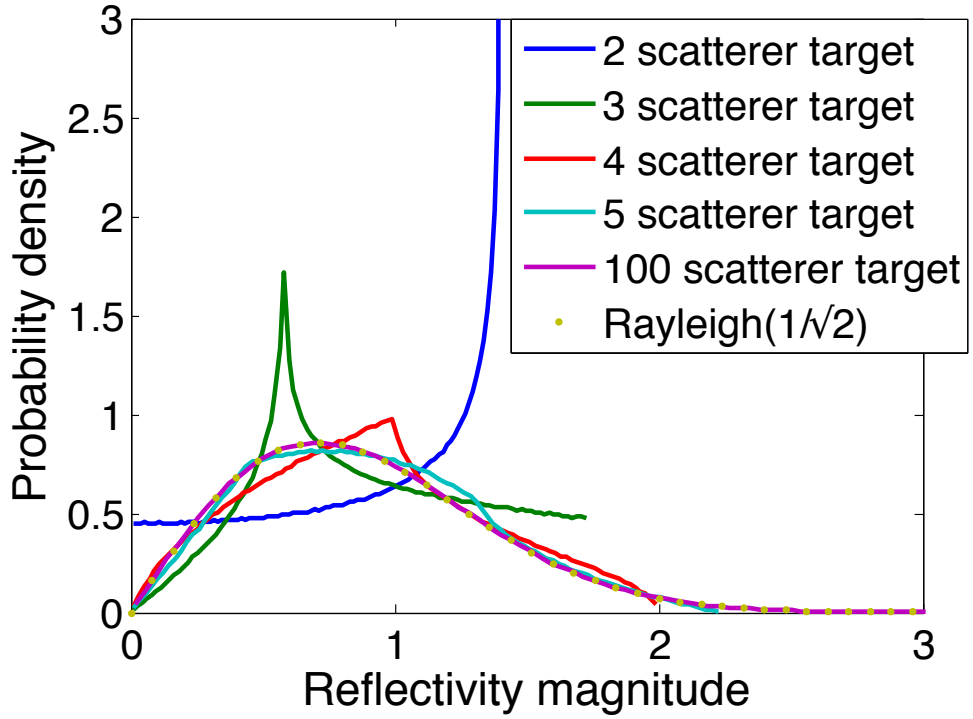

Fig. 3. Reflectivity probability density functions of a Q scattering points target with $Q = 2, 3, 4, 5$ & 100 using the scatterer reflectivity model from Eq. (15).

We also notice in Fig. 3 that while the convergence of the reflectivity distribution function to a Rayleigh distribution is fast, the reflectivity of a target with few scattering points ($Q \in [2, 3, 4]$) presents a very characteristic PDF. The small number scatterer targets are particularly interesting because they are more likely to represent simple shaped man-made target (cf. section III).

Monostatic sonar systems only provide one observation of the target per cycle. With MIMO systems however, assuming widely separated antennas, we have access to $N = K \times L$ independent observations, where K is the total number of transmitters and L the total number

of receivers. The question we are asking here is: Can we estimate the number of scattering points of a target with a large MIMO system? If yes, how many observations (N) are needed to estimate the scattering point density?

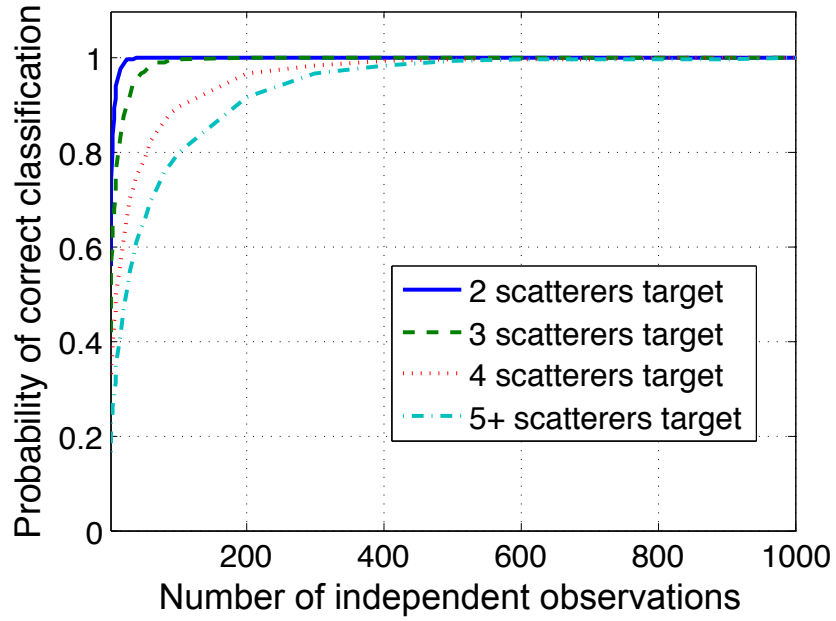

(a)

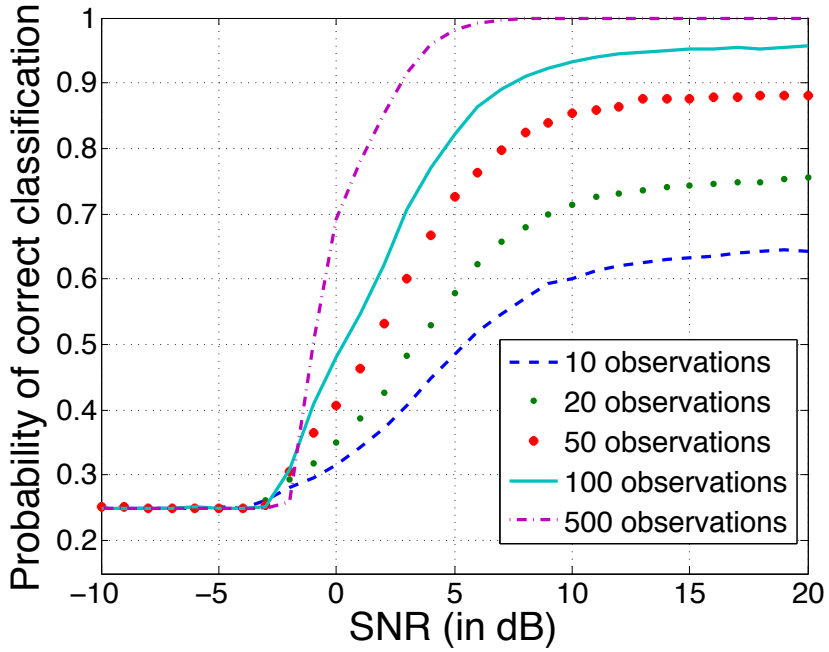

(b)

Fig. 4. (a) Correct classification probability against the number of independent observations for 4 classes of targets (2, 3, 4 and 5+ scattering points targets). (b) Overall correct classification probability against SNR for MIMO sonar systems with 10, 20, 50, 100 and 500 independent observations.

Here we want to take advantage of the dissimilarities of the probability density functions to estimate the number of scattering points. Each observation is a realisation of the random variable $\gamma_n = \sqrt{\left|\sum_{q=1}^{Q} h_{lk}^{(q)}\right|^2}$ with Q the number of scattering points. Each set of observations $\Gamma = \{\gamma_n\}_{n\in[1,N]}$ represents the MIMO output (N is the total number of observations). Given a set of observations Γ we can compute the probability that the target has Q scatterers using Bayes rules:

$$\mathrm{P}(T_Q|\Gamma) = \frac{\mathrm{P}(\Gamma|T_Q)\mathrm{P}(T_Q)}{\mathrm{P}(\Gamma)} \tag{17}$$

where T_Q represents the event that the target has Q scatterers. Assuming the independence of the observations $\mathrm{P}(\Gamma|T_Q)$ can be written as:

$$\mathrm{P}(\Gamma|T_Q) = \prod_{n=1}^{N} \mathrm{P}(\gamma_n|T_Q) \tag{18}$$

$\mathrm{P}(\gamma_n|T_Q)$ is computed thanks to the reflectivity density function presented in Fig. 3. We consider 4 target types: 2 scatterer target, 3 scatterer target, 4 scatterer target and 5+ scatterer target. So $Q \in \{2, 3, 4, 5+\}$. Therefore we can write:

$$\mathrm{P}(\Gamma) = \sum_{Q=2}^{5} \mathrm{P}(\Gamma|T_Q)\mathrm{P}(T_Q) \tag{19}$$

Given that we have no *a priori* information about the target we can assume that $\mathrm{P}(T_Q)$ is equal for all target class T_Q. Eq. (17) then becomes:

$$\mathrm{P}(T_Q|\Gamma) = \frac{\prod_{n=1}^{N} \mathrm{P}(\gamma_n|T_Q)}{\sum_{Q=2}^{5+} \mathrm{P}(\Gamma|T_Q)} \tag{20}$$

The estimated target class corresponds to the class which maximises the conditional probability given by Eq. (20).

To validate the theory, a number of experiments have been run in simulation. In a first experiment, 10^6 classification tests have been computed for MIMO sonar systems whose independent observations varies from 2 to 1000. Note that these simulations have been run with a 10dB SNR. Fig. 4*(a)* draws the probability of correct classification for each

class depending on the number of observations. The first remark we can make is that it is possible to estimate the number of scattering points in a target if the number of scatterers is low (≤ 4). The 2 scattering point target can be seen as a dipole and its reflectivity PDF differs considerably from any n scattering points target (with $n \geq 2$). For this reason fewer independent observations are needed to correctly classify this class of target. With only 10 observations, a 2 scattering point target is correctly classified in 96% of cases. Table I provides the overall classification using our PDF matching algorithm depending on the number of independent observations. Only 100 independent observations are needed to reach an overall 92% correct classification.

number of observations	correct classification
10	64%
50	86%
100	92%
200	97%
500	99.81%
1000	>99.999999 %

TABLE I
OVERALL CORRECT CLASSIFICATION DEPENDING ON THE NUMBER OF OBSERVATIONS.

In second set of experiments, we computed the ATR (Automatic Target Recognition) performance against noise. The MIMO observations were corrupted by an independent additive Rayleigh noise with a SNR varying from -10 to 20dB. Fig. 4*(b)* displays the probability of correct classification using the conditional probability maximisation from Eq. (20) against the SNR level for MIMO systems with 10, 20, 50, 100 and 500 independent observations. The bayesian classifier is based on matching target amplitude level to given probability density functions. So it is not surprising that a certain SNR level is needed. In Fig. 4*(b)*, the probability of correct classification stabilised at around 10dB SNR. The surprising factor came from the fact that the classifier starts to perform better than random (25% correct classification) at a negative SNR (around -3dB). With 500 observations and 0dB SNR, the classifier reaches 70% of correct classification.

The ATR performances of spatially distributed MIMO systems came from the multiplicity of observations in a single snapshot. As long as the observations are statistically independent,

such systems can provide meaningful statistical information about the target such as its PDF. We showed in this section an example of how to use this information to classify target based on its number of scatterers, Note that the important factor in the MIMO recognition capability is the independence of the observations. We develop and quantify this assumption in section IV-C.

B. The detection problem with statistical MIMO

The usual approach to the detection problem consists in evaluating the presence of a target of interest in the received signal $\mathbf{r}$. Under the null hypothesis $\mathcal{H}_0$ the received signal $\mathbf{r}$ contains only the noise $\mathbf{n}$. Under the target presence hypothesis $\mathcal{H}_1$ the received signal contains both the target signal and the noise. A detection rule function $\mathcal{F}(\mathbf{r})$ is compared to a given threshold η. If $\mathcal{F}(\mathbf{r}) < \eta$, the hypothesis $\mathcal{H}_0$ is chosen; if $\mathcal{F}(\mathbf{r}) \geq \eta$, hypothesis $\mathcal{H}_1$ is chosen. We can distinguish two kinds of errors:

- the *false alarm*: the detector detects a target ($\mathcal{F}(\mathbf{r}) \geq \eta$) when no target is present.
- the *missed detection*: the detector misses a target ($\mathcal{F}(\mathbf{r}) < \eta$) when a target is present.

In the rest of this section we compute the detection rule function $\mathcal{F}(\mathbf{r})$ under the hypothesis made in section II.

Let $r_l(t)$ be the total received signal at the receiver l. According to our previous notations we have:

$$r_l(t) = \sum_{k=1}^{K} z_{lk}(t) \tag{21}$$

where $z_{lk}(t)$ has been defined in Eq. (5). Let $\mathbf{x}$ be the $KL \times 1$ output vector from the filter bank $s_k^*(t)$ with $k \in [1, K]$. Note that $\mathbf{x}$ represents the match-filtered response and is computed as followed:

$$[\mathbf{x}]_{(l-1)L+k} = r_l \star s_k^*(t) \tag{22}$$

We assume that all the emitted pulses $s_k(t)$ are orthogonal so:

$$s_i \star s_j^*(t) = \delta(i-j) \tag{23}$$

where δ denotes the discrete Dirac delta function. Note that MIMO waveform design for radar is still a very active part of research. If in practice purely orthogonal waveforms do

not exist, different approaches were developed to minimise the waveform cross-correlation including time, frequency or code divided approaches. The study of orthogonal waveforms however is beyond the scope of this paper and the reader can refer to [34]–[37] for more information on the subject.

Using Eq. (23) into Eq. (22) we arrive to:

$$\begin{aligned}[\mathbf{x}]_{(l-1)L+k} &= r_l \star s_k^*(t) \\ &= \sum_{k=1}^{K} z_{lk} \star s_k^*(t) \\ &= z_{lk} \star s_k^*(t) \\ &= \sum_{q=1}^{Q} h_{lk}^{(q)} \end{aligned} \tag{24}$$

We choose the following detection rule:

$$\mathcal{F}(\mathbf{r}) = \frac{1}{N}||\mathbf{x}||^2 = \frac{1}{N}\sum_{l,k}||x_{lk}||^2 \tag{25}$$

where $N = K \times L$ represents the total number of observations provided by the MIMO system. Using the same probability distribution stated in the model presented in section IV-A, we deduce that under the $\mathcal{H}_1$ hypothesis, $\mathcal{F}(\mathbf{r})$ has the following probability distribution:

$$\mathcal{F}(\mathbf{r}) \sim \frac{1}{N}\sum_{n=1}^{N} \text{Rayleigh}^2(\sigma) \tag{26}$$

Using the properties of the Rayleigh distribution we can write:

$$\sum_{n=1}^{N} \text{Rayleigh}^2(\sigma) \sim \Gamma(N, 2\sigma^2) \tag{27}$$

where Γ is the Gamma distribution. So the PDF of the detection rule $\mathcal{F}(\mathbf{r})$ is $N.\Gamma(Nx, N, 1)$. The asymptotic behaviour of the detection rule $\mathcal{F}(\mathbf{r})$ can be deduced from the following identity:

$$\lim_{N\to+\infty} N.\Gamma(Nx, N, 1) = \delta(1-x) \tag{28}$$

The convergence of the detection rule $\mathcal{F}(\mathbf{r})$ is shown in Fig. 5.

The proof of Eq. (28) is given in the appendix. Eq. (28) has interesting consequences: as

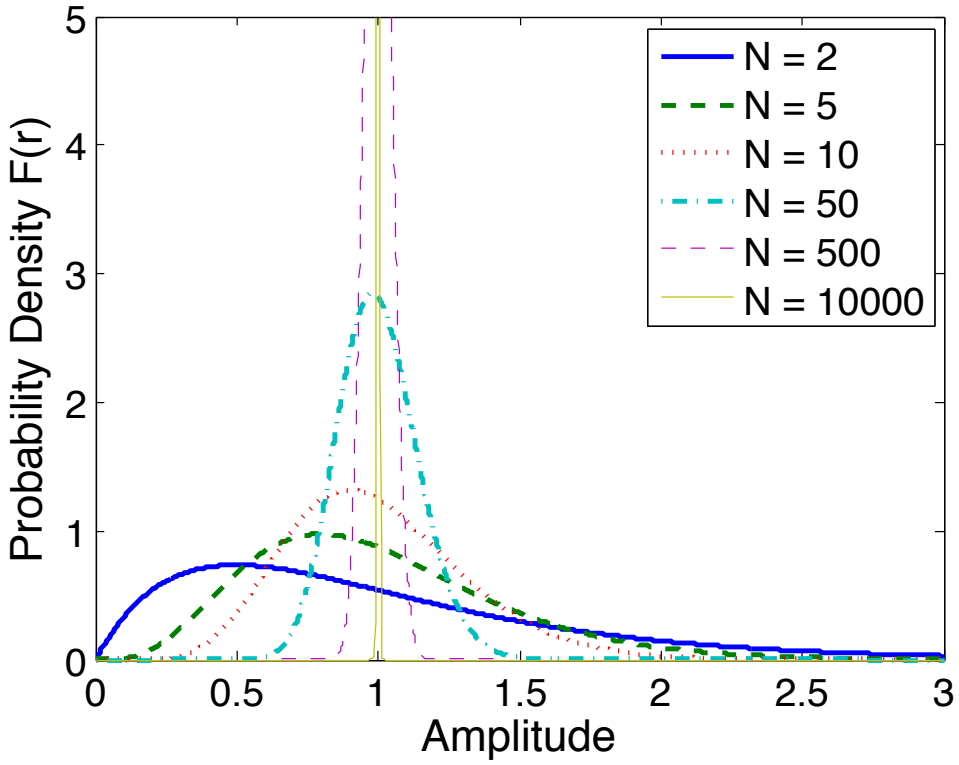

Fig. 5. Probability density function of $N.\Gamma(Nx, N, 1)$ for several values of N.

the total number of observations N offered by the MIMO system increases, the probability density function of the detection rule $\mathcal{F}(\mathbf{r})$ under the $\mathcal{H}_1$ hypothesis tends to the Dirac function δ_1. As a consequence the random variable $\mathcal{F}(\mathbf{r})$ representing the target intensity averaged over all the MIMO observations collapses to a real number: the average RCS defined in section II-A.

Haimovich [3] defines the average radar cross section as $E[\Sigma\Sigma^T] = 1$. This definition implies that the contribution of all the scatterers sum incoherently. Considering a target contained within a single resolution cell and assuming coherent sensors such radar or sonar the scattering points interact coherently with each other from a signal point of view. The random summation creates constructive and destructive interferences as explained with the Random Walk analogy in section IV-A. We can then define the *effective* RCS as the effective average reflectivity of the target viewed by the sensors. We also demonstrated that we can

very accurately model the *effective* RCS of a target with more than 5 scatterers by:

$$E\left[\text{Rayleigh}(\sigma)\right] = \sigma\sqrt{\frac{\pi}{2}} \tag{29}$$

where $\sigma = 1/\sqrt{2}$. So the *effective* RCS of the target is in fact:

$$E[\{X_q\}] = \sqrt{\pi}/2 \tag{30}$$

It is important to note that $E[\{X_q\}] < 1$.

For this precise reason the result given by Eq. (28) appears counter-intuitive. We would have expected the detection rule function $\mathcal{F}(\mathbf{r})$ to tend to the mean of this Rayleigh distribution *i.e.* $\sqrt{\pi}/2$ which represents the effective RCS defined earlier. The asymptotic behaviour of $\mathcal{F}(\mathbf{r})$ gives a new insight into the capabilities of MIMO systems. It demonstrates indeed that as the number of independent observations increases the MIMO detection system decorrelates the contribution of each scatterer in the echo signal and in fact solves the speckle noise in the target response. Figure 5 shows the convergence speed of Eq. (28). Note that the convergence is relatively slow (especially when compared to the convergence speed of Eq. (16)). This figure seems to indicate that roughly 100 observations are necessary to decorrelate scatterers within one pixel resolution.

C. Super-resolution capabilities of coherent MIMO systems

In the previous section we derived an important result: with a sufficient number of independent observations, MIMO systems can decorrelate the scatterers contributions within one pixel resolution. It is in that sense that we understand the notion of "*super-resolution*": all the scatterers within one resolution cell decorrelate from each other. In other words, no artefacts induced by the imaging a one scatterer (e.g. sidelobes) will disrupt the imaging of the other scatterers. Super-resolution can then be achieved using MIMO systems under certain conditions. So far we have not taken into account the geometry of the target. We can reasonably assume that a target has a fixed geometry during the MIMO inspection. In this section we intend to recover the target geometry via imaging. In the previous sections IV-A and IV-B we analysed the MIMO signals as statistical data. As the aim is now to image the

target, we need to introduce the geometry of the MIMO sonar systems within its environment (*i.e.* the Tx and Rx locations). An observation is then linked to a particular configuration in the space, and each MIMO pair provides a view of the target. We then define independent views as:

Two views are independent if and only if their respective observations of a scene are statistically independent.

With the insight of the previous results we know that to achieve super-resolution the following conditions must be respected:

- Independent views: the antenna have to be sufficiently spaced to ensure the independence of each view.
- Decorrelation: the total number of views has to be large enough to ensure the scatterers decorrelation.
- Broadband: in order to achieve the range resolution needed, the MIMO system has to use broadband pulses for range compression.

So far we have assumed that all the MIMO observations were independent. This hypothesis was necessary for MIMO systems to achieve the recognition capability presented in section IV-A and to solve the target speckle (cf. appendix). We stipulated that the antennas have to be sufficiently separated to ensure the independent view assumption. In the next paragraphs we quantify the separation required to ensure independence and develop independence measure for MIMO systems depending on its geometry.

By introducing the term *view* we implicitly introduce the geometry and the configuration of the MIMO system. Let θ be the view angle of the transmitter and ϕ the view of the receiver. The bistatic configuration of a transmitter/receiver pair of the full MIMO system is drawn in Fig. 6 and will be noted (θ, ϕ). We are interested here in knowing the level of independence of a view $V(\theta_1, \phi_1)$ with another view $V(\theta_2, \phi_2)$. To measure the dependence of 2 random variables the Pearson product-moment correlation coefficient or correlation coefficient is commonly used [38]. However the correlation coefficient is not adequate here: First, this coefficient has been designed with a normal distribution assumption, and this assumption does not hold in our case. Second, this coefficient only measures linear correlation between the random variable. Finally, this coefficient is not a real independence measure in the sense

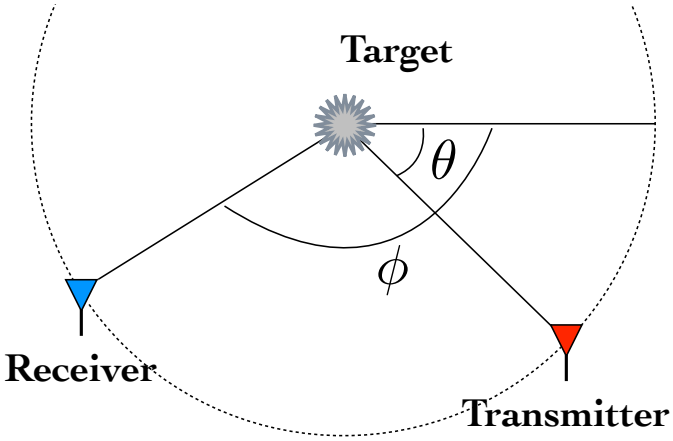

Fig. 6. Bistatic configuration. θ represents the view angle of the transmitter and ϕ the view angle of the receiver.

that the correlation coefficient of 2 random variables can be null even if these random variables are dependent. To overcome this we propose to use the distance correlation introduced by Székely in [23]. Székely defines the distance covariance $\mathcal{V}$ as:

$$\mathcal{V}^2 = \frac{1}{c_p c_q} \int_{\mathbb{R}_{p+q}} \frac{|f_{X,Y}(t,s) - f_X(t) f_Y(s)|^2}{|t|_p^{1+p} |s|_q^{1+q}} dtds \tag{31}$$

where f_X and $f_{X,Y}$ represent respectively the characteristic and the joined characteristic function of X or (X,Y), p and q are respectively the dimensions of the random vector X and Y, and c_d is defined as follows:

$$c_d = \frac{\pi^{(1+d)/2}}{\Gamma((1+d)/2)} \tag{32}$$

where $\Gamma(.)$ is the full gamma function. For $\mathcal{V}^2(X)\mathcal{V}^2(Y) \neq 0$ the distance correlation is then defined as:

$$\mathcal{R}^2(X,Y) = \frac{\mathcal{V}^2(X,Y)}{\sqrt{\mathcal{V}^2(X)\mathcal{V}^2(Y)}} \tag{33}$$

Székely shows in [23] that $\mathcal{R}$ has "the properties of a true dependence measure" and in particular that two random vectors X and Y are independent if and only if $\mathcal{R}(X,Y) = 0$.

To assess the inter views dependence of a MIMO system, 10^4 targets with 2, 3, 4 or 5 scatterers were randomly generated. All the targets are contained in a cell of 3λ radius.

Note that this MIMO system has a central frequency of $f_0 = 100$kHz and a bandwidth of $\Delta f = 40$kHz. We will use this configuration for all the simulations within this section. For each target, its response V was computed as a function of the transmitter and receiver view angle (θ, ϕ). Each pair (θ, ϕ), $V(\theta, \phi)$ can then be considered as a random vector. The distance correlation $\mathcal{R}$ between all pairs $(\theta_n, \phi_n) \in [-\pi, \pi]^2$ is then computed. For the view angles (θ_0, ϕ_0), let $\mathcal{A}_0$ be the matrix defined by:

$$\mathcal{A}_0(\theta, \phi) = \mathcal{R}(V(\theta_0, \phi_0), V(\theta, \phi)) \tag{34}$$

Note that in the point scatterer model there is a symmetry between the transmitter and the receiver and $V(\theta, \phi) = V(\phi, \theta)$. For this reason the matrix $\mathcal{A}_0$ is symmetric along its first diagonal.

Let $\theta_1 = \theta_0 - \alpha$ and $\phi_1 = \phi_0 - \alpha$. Thanks to the axial symmetry of the problem we can write that:

$$\mathcal{A}_0(\phi, \theta) = \mathcal{A}_1(\phi - \alpha, \theta - \alpha) \tag{35}$$

So $\mathcal{A}_0(\theta, \phi)$ can be computed for only one θ_0. We chose $\theta_0 = 0$. For display purposes we display in Fig. 7 the distance correlation matrix $1 - \mathcal{A}_0(\theta, \phi)$ for $\phi_0 = 0$, $\phi_0 = \pi/2$ and $\phi_0 = \pi$.

Fig. 7(a) displays the monostatic case, the transmitter and the receiver are in the same position: $\theta_0 = \phi_0 = 0$. Even though the monostatic configuration is convenient from a practical point of view it does not offer the best view in term of correlation. The monostatic view correlates strongly with its neighbours $(\theta = +\alpha, \phi = -\alpha)$ for $\alpha \in [-25°, +25°]$. It is interesting to note that the monostatic view correlates as well with $(\theta = \alpha, \phi = \alpha)$ for $\alpha \in [-6°, +6°]$. So if we consider a monostatic sonar turning around the target for a full 360°, an average of 30 independent views will be obtained which is insufficient to achieve super-resolution.

In Fig. 7(b) the target is in-between the transmitter and the receiver. Although this configuration is not practical as the transmitted wave will arrive at the same time as the target echo to the receiver, it is interesting to note that all the opposite views $(\theta, \theta + \pi)$ for all θ correlate strongly.

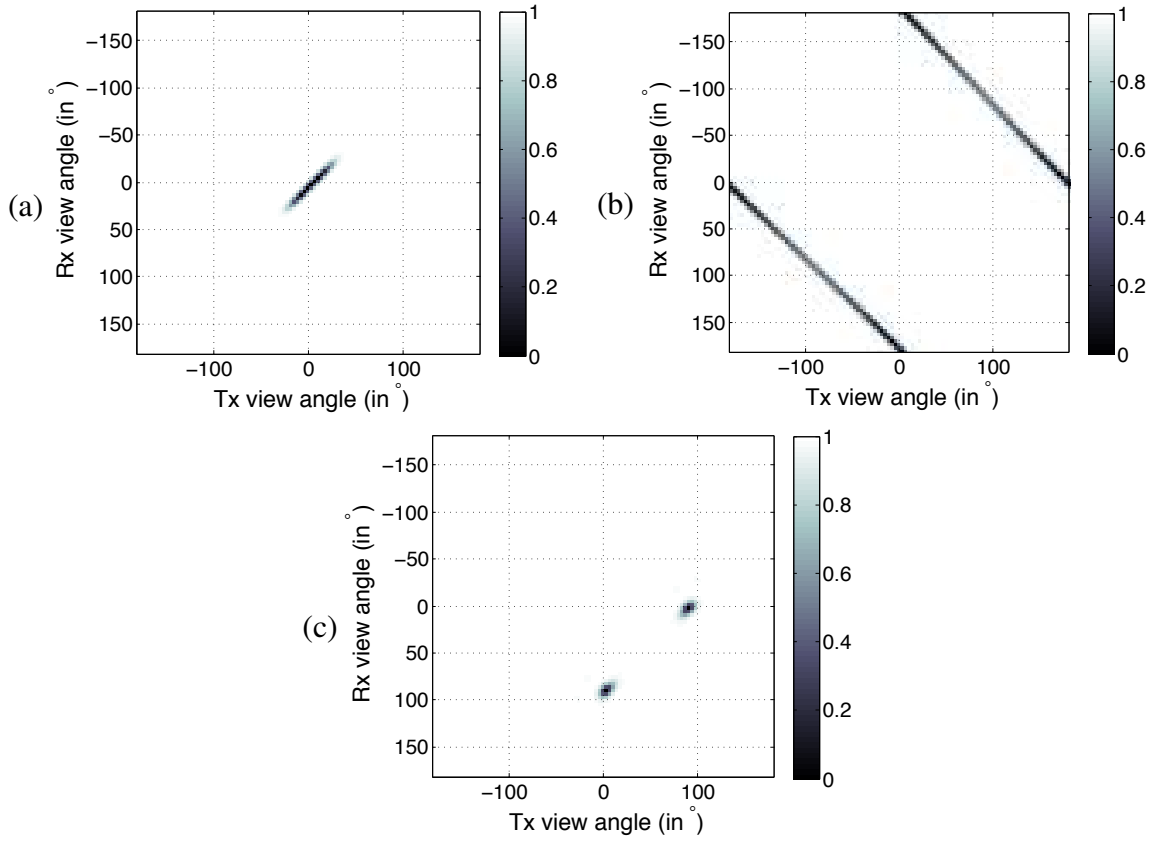

Fig. 7. Distance correlation matrix $1 - \mathcal{A}_0(\theta, \phi)$ for (a): $\phi_0 = 0$, (b): $\phi_0 = \pi$ and (c): $\phi_0 = \pi/2$.

In Fig. 7(c) displays the distance correlation matrix with $\phi_0 = \pi/2$. As predicted we observe a symmetry along the first diagonal and $\mathcal{A}_0(\theta, \phi) = \mathcal{A}_0(\phi, \theta)$. The correlation peaks are focused on (θ_0, ϕ_0) and (ϕ_0, θ_0). This configuration is the most effective as far as its independence is concerned. And the independence of this view toward its neighbours is maximised.

It is important to note that these results are dependent of the frequency used and the size of the cell. It can be shown that increasing the frequency and/or the cell narrow the peaks of Fig. 7(c). The potential number of independent views will then increase. The derivation of this result however goes beyond the scope of this manuscript.

In the following simulation we aim to demonstrate that we can recover the geometry of a target (*i.e.* the location of its scatterers). Given the results presented in Fig. 7 we chose a "L" shape MIMO configuration as pictured in Fig. 8. The transmitters are placed along the x-axis, the receivers are on the y-axis. For this experiment the transducers are placed at

an equal spacing along the axis. The number of transmitters and receivers and the spacing between them is adjustable. The central frequency of the MIMO sonar system is 100kHz with a frequency band of around 40kHz. We consider a 3 point scatterers target centred at the point (x=20m, y=20m), the scatterers are separated by one wavelength which corresponds to 1.5cm. Each scatterer has a reflectivity of $\frac{1}{\sqrt{3}}$.

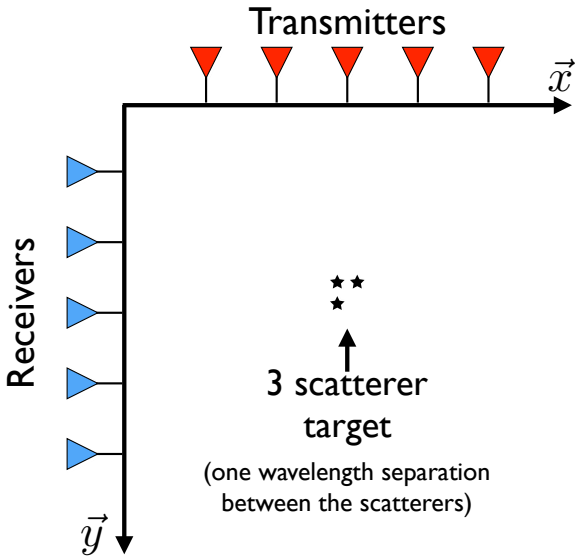

Fig. 8. MIMO configuration.

In order to image the output of the MIMO system we will use the multi-static back-projection algorithm which is a variant of the bistatic back-projection algorithm developed by the SAR community. Further details can be found in [39]–[41]. Using the back-projection algorithm the SAS image is computed by integrating the echo signal along a parabola. In the bistatic case the integration is done along ellipses. For the multi-static scenario the continuous integration is replaced by a finite sum in which each term corresponds to one transmitter/receiver pair contribution. It is worth mentioning that, due to its sparse geometry, the MIMO imagery processing, using traditional back projection techniques, will potentially develop grating lobes, which can be significant if the spatial sampling is regular. This problem is included into the more general imagery problem, or how to form a MIMO image. The subject is extremely vast and beyond the scope of this manuscript.

In Fig. 9(a) the MIMO image using incoherent processing is reconstructed (*i.e.* only the amplitude of the echoes have been used in the multi-static back-propagation algorithm). This

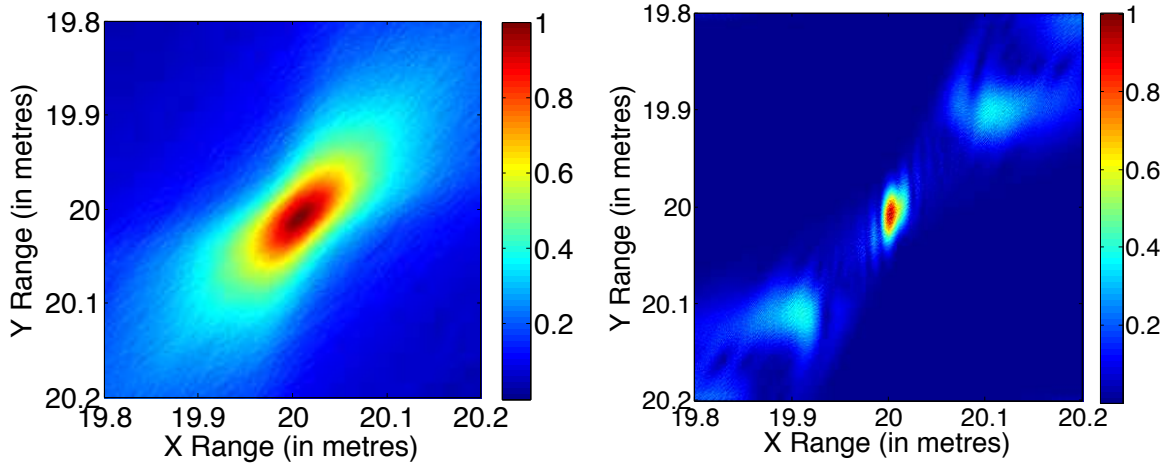

Fig. 9. 3 scatterers target MIMO image using: (a) 10 Tx, 10 Rx with incoherent processing, (b) SIMO with 1 Tx and 10 Rx with 3 m spacing.

figure represents in essence how the MIMO signal has been treated so far: the detection processing has been done using only the amplitudes of the different views. As expected the 3 scatterer target is represented only as blob of energy. Note that the dimensions of this patch of energy represent the resolution limit of the incoherent system which is approximately 10 cm $\times$ 10 cm.

For comparison purposes, we plot in Fig. 9(b) the target image obtained using a SIMO system with the same receiver array of 10 receivers with 3 m spacing but only 1 transmitter. With only 10 independent views, the scatterers within the target are unresolved and only a blob of energy is visible.

In Fig. 10(a) we have considered a MIMO system with 10 transmitters and 10 receivers with a spacing of 20 cm. For this scenario the 20 cm spacing breaks the widely spaced antenna assumption and the views are not exactly independent from each other. For this reason we only observe a blob of energy at the target location.

In Fig. 10(c) the MIMO system consists of 3 transmitters and 3 receivers with 3 metres spacing. In this case the spacing between the antennas is several hundreds of wavelengths so the independence of the views is respected. The total number of views however is 3 $\times$ 3 = 9 independent views which is relatively low according to the convergence speed of Eq. (28). In this scenario the number of views is too low to ensure the decorrelation of the scatterers

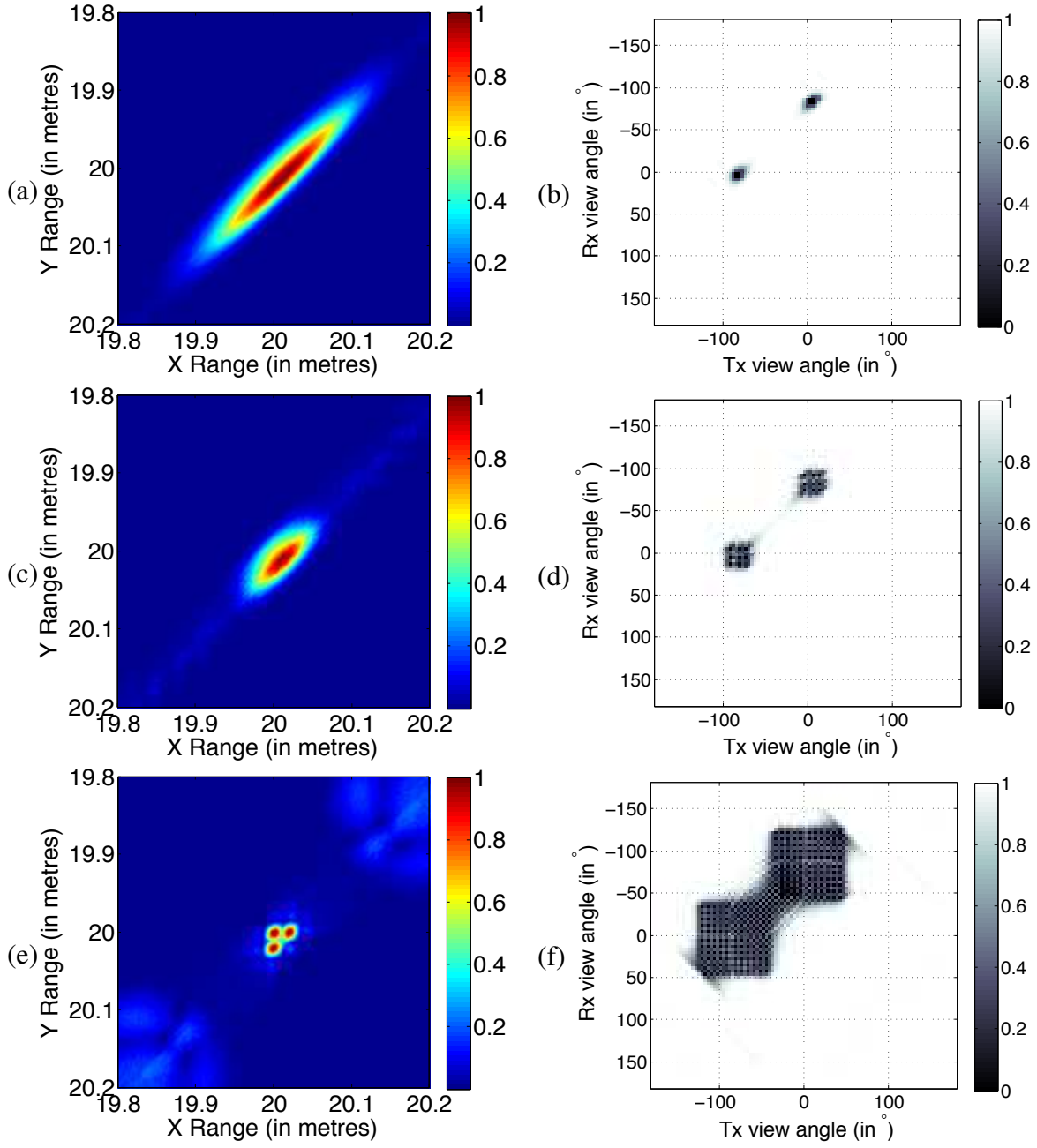

Fig. 10. MIMO target image given by and full MIMO inter-correlation distance matrix $1 - \mathcal{B}(\theta, \phi)$ of (a)-(b) 10 Tx and 10 Rx with 20 cm spacing, (c)-(d) 3 Tx and 3 Rx with 3 m spacing, and (e)-(f) 10 Tx and 10 Rx with 3 m spacing.

within the target. For this reason only a blob of energy marks the target location. However by closely inspecting to the central blob it is possible to distinguish a structure.

Finally in Fig. 10(e) we consider a MIMO system with 10 transmitters and 10 receivers with a spacing of 3 metres. With this configuration we respect the conditions stipulated earlier and we are able to clearly image the 3 scatterer target in so doing achieve super resolution

imaging.

It is interesting to compare these results to the intra-views correlation of the different MIMO systems. Let note $\{(\theta_n, \phi_n)_{n\in[1,N]}\}$ the views of the MIMO system. The level of inter-correlation for the full MIMO can be computed as:

$$\mathcal{B}(\theta, \phi) = \max_{n\in[1,N]} \mathcal{A}_n(\theta, \phi) \tag{36}$$

In Fig. 10(b), (d) and (f), we plot the $1 - \mathcal{B}(\theta, \phi)$ functions for the same MIMO configurations as the ones explained in Fig. 10. In Fig. 10(b) we are considering the 10×10 MIMO system with 20 cm separation between antennas. The 100 views produced by this configuration are all concentrated around the (0°,-90°) view and are clearly all correlated to each other. The independent views assumption breaks down. In Fig. 10(d) the 3×3 MIMO configuration is considered. The 3 m spacing between the antenna ensures view independence and we can clearly see in the cluster 9 peaks corresponding to each view. In Fig. 10(f) the 10×10 MIMO configuration is considered. Again the 3 m antenna separation provide the necessary independence between the views and the 100 correlation peaks are visible and distinct between each other. The $\mathcal{B}(\theta, \phi)$ inter-correlation distance matrix then gives us an insight on how to design an efficient MIMO system and ensure the views independence. Assuming that the MIMO system provides enough views for recognition or super-resolution, each view (θ_n, ϕ_n) in the $\mathcal{B}(\theta, \phi)$ should decorrelate as much as possible with the other views $(\theta_m, \phi_m)_{m\neq n}$.

In a second simulation we aim to evaluate the distance resolution of the 10×10 MIMO system with 3m spacing as described in Fig. 10(e) by imaging two scatterers at 20m range and separated by a distance d. Figure 11 provides a waterfall plot of the cross section of the 2 scatterers MIMO image for a distance separation between 0 and 20mm. The MIMO system is able to separate 2 scatterers separated by 6mm. To put this number into perspective it is interesting to compute the maximum range resolution $c/2\Delta f$ where c is the speed of sound in water and Δf the bandwidth of the pulse. In our case the resolution in range is then around 2cm. For the resolution in cross range, the theory predicts a resolution of $(k_{\max} - k_{\min})/c$. Here, we have $f_{\min} = 80$kHz and $f_{\max} = 120$kHz which results in a resolution of around

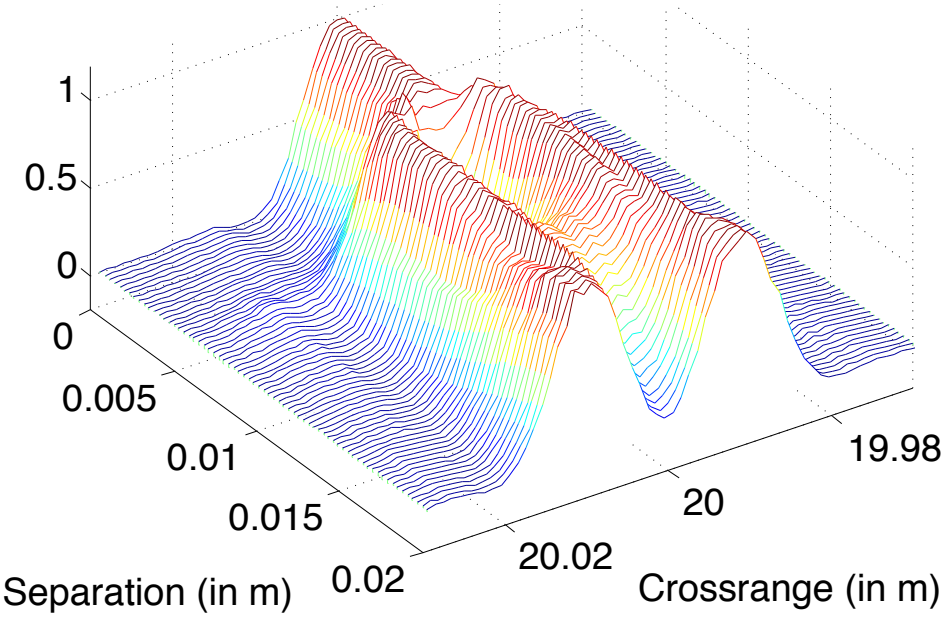

Fig. 11. Waterfall plot of the cross section of the 2 scatterers MIMO image for a distance separation between 0 and 20mm.

3.75cm. Eq. (28) predicts statistically the super resolution capability of MIMO systems. With this simulation we show that large MIMO system can achieve at least 3.5 times better resolution that other traditional systems.

For comparison purposes we have computed the SAS image of the same target as described in Fig. 8 using the same frequency band and at the same range as in the previous experiment. The SAS image of the target is displayed in Fig. 12.

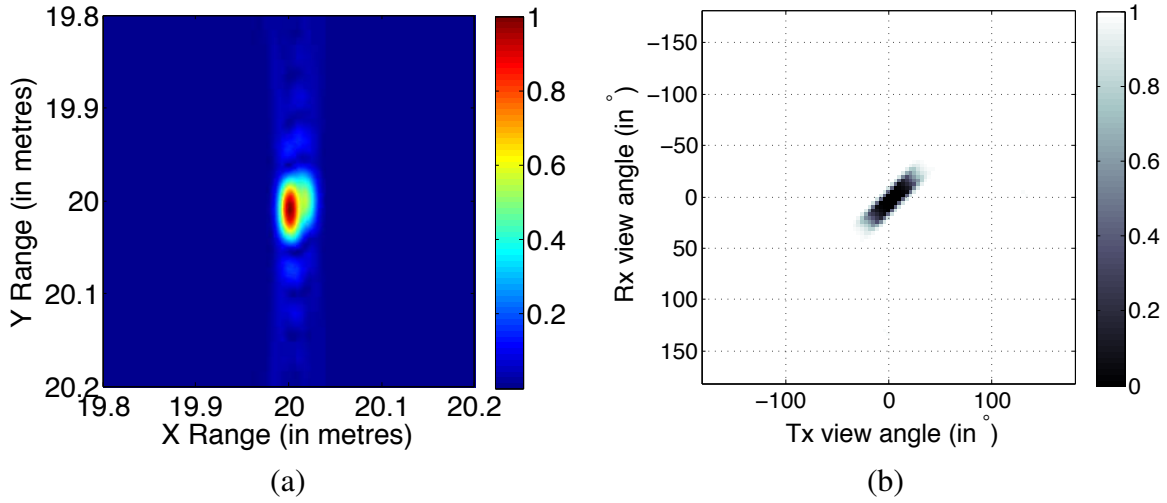

Fig. 12. 3 scatterers target using SAS system. (a) SAS image, (b) $1 - \mathcal{B}(\theta, \phi)$ function for the SAS configuration.

The SAS system runs in a straight line along the y-axis at 20m range from the target. Using the phase center approximation, the SAS is seen as a single-channel system and the target echoes are computed at every $\lambda/2$ along the synthetic antenna. In Fig. 12(a), the beamwidth is fixed to 10°. Note that the choice of a 10° beamwidth for this simulation was inspired by the 7° beamwidth of the MUSCLE SAS system from CMRE. In total 467 echoes are computed and the SAS image is formed using back-propagation algorithm. Despite the high number of views and because all the SAS subviews are highly correlated as shown in Fig. 12(b), the SAS system fails to separate the 3 scatterers. Using the same model and parameters as described in section IV-C we can infer that monostatic systems correlate in average for 12°. With a 10° beamwidth, a SAS system then sees at most 2 to 3 independent views of the target. Note that on this aspect the SAS image reconstruction is based on the hypothesis that each pixel contains one scatterer. SAS systems requires strong correlation between consecutive views in order to track and correct the echoes phase changes. So in that aspect it is not surprising that the mono-views from SAS systems are so strongly correlated to each other.

Of course the SAS system used in the previous experiment has a much smaller aperture than the 10×10 MIMO system described earlier. For the next experiment, we consider four scatterers target. Each scatterer is located at a vertex of a square whom size is $\lambda/2$. For the SAS system, we consider a circular SAS target acquisition at 20m range from the target. For the MIMO system, we consider a 40×40 MIMO system. We call element a collocated transmitter and receiver. 10 elements with 3m spacing are placed on the axis x=0m, 10 on the y=0m axis, 10 on the x=40m line and finally 10 on the y=40m line.

The 360° SAS aperture provides in that case a total of 16756 echoes. These echoes are processed using a back-projection algorithm modified for the circular acquisition to form the image pictured in Fig. 13(a). Despite the maximum aperture of the SAS, the sidelobes induced by the proximity of the scatterers greatly deteriorate the image. The four scatterers are visible but barely distinguishable from their sidelobes. One can count five or even nine potential scatterers. Fig. 13(b) shows the MIMO image of the target. The target is resolved and the four scatterers are clearly separated. We estimated that the circular aperture of the SAS system provides approximately 35 independent views of the target. The 16756 SAS echoes are

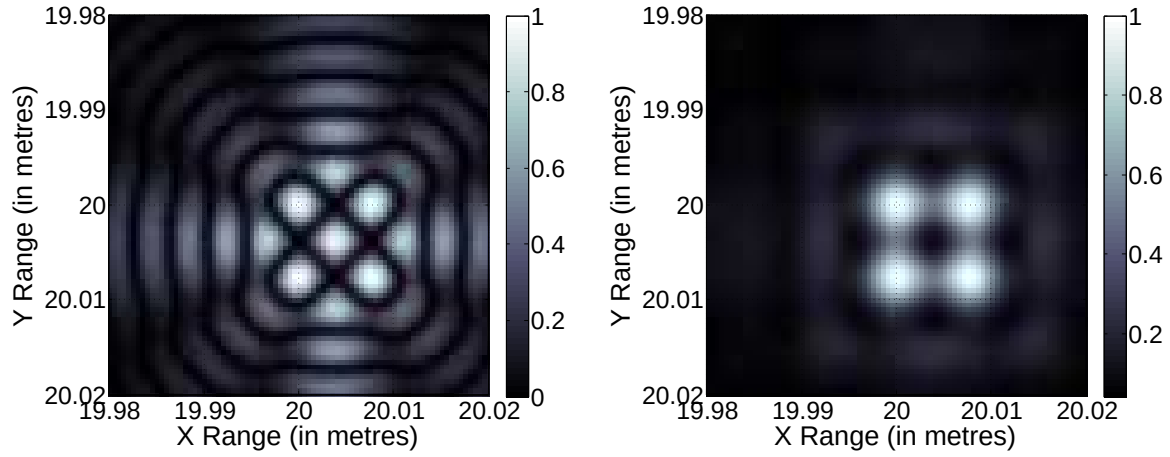

Fig. 13. Four scatterers target imaged with (a) circular SAS, (b) 40 $\times$ 40 MIMO system.

not statistically sufficient to fully resolve this specific target. The MIMO structure described above however provides around 1300 independent views which is enough to resolve the target. By carefully designing the MIMO system, we were able to provide enough independent views for the target to be properly imaged. In this instance, MIMO provides better imagery and more resolution than the SAS system.

V. Conclusion

In this paper we have studied the fundamental principles of MIMO sonar systems. We have proposed a new formulation for broadband MIMO sonar systems by separating clearly the terms of propagation and the terms of target reflection. This formulation is more flexible than the one proposed by the radar community for different target model integration. The main advantage of statistical MIMO systems is to procure in a single snapshot a large number of independent views of a target of interest. The multiple independent observations can provide useful statistics of the target such as its PDF for example. We showed in this paper an example of how to use the MIMO signal and developed an algorithm to determine the number of scatterers contained in a target and then demonstrated the recognition capability of MIMO systems. Finally we have explained why well designed MIMO systems can achieve super-resolution and in certain cases surpass the resolution of SAS systems. By highlighting the fact that it is the independence between the views that makes MIMO sonar systems

attractive we provided guidelines to how and where the transmitters and receivers should be placed. The MIMO sonar capabilities described in this paper make such a system a very attractive tool for surveillance. In a fixed environment such as an harbour or a narrow channel the transmitters and receivers elements can be carefully placed to ensure coverage and view independence. The recognition capabilities of MIMO sonar can then be used be identify threats.

APPENDIX

PROOF OF THE CONVERGENCE OF EQUATION 28

We demonstrate here the result given by equation (28). We stipulated that:

$$\lim_{N\to+\infty} N.\Gamma(Nx, N, 1) = \delta(1-x) \tag{37}$$

where $\Gamma(x, k, \theta)$ represents the Gamma distribution function and $\delta(x)$ the Dirac function. The Gamma distribution function is defined as follows:

$$\Gamma(x, k, \theta) = x^{k-1}\frac{\mathrm{e}^{-x/\theta}}{\theta^k\Gamma(k)} \tag{38}$$

with $x \geq 0$ and $k, \theta > 0$ and $\Gamma(k)$ represents the Gamma function. Note that $\Gamma(x, k, \theta) > 0$. In our case we are looking at the convergence of:

$$\begin{aligned} N.\Gamma(Nx, N, 1) &= N(Nx)^{N-1}\frac{\mathrm{e}^{-Nx}}{\Gamma(N)} \\ &= \frac{N^N}{\Gamma(N)\mathrm{e}^N}.\frac{(x\mathrm{e}^{1-x})^N}{x} \\ &= A(N)f(x, N) \end{aligned} \tag{39}$$

where $A(N) = \frac{N^N}{\Gamma(N)\mathrm{e}^N}$ and $f(x, N) = (x\mathrm{e}^{1-x})^N/x$. Note that $A(N)$ represents a normalization factor and for all N:

$$\int_{x=0}^{+\infty} x^{N-1}\mathrm{e}^{N(1-x)}dx = \frac{1}{A(N)} \tag{40}$$

Asymptotic behaviour of $A(N)$

To get the asymptotic behaviour of $A(N)$, we use the Stirling formula:

$$n! \sim \sqrt{2\pi n}\left(\frac{n}{\mathrm{e}}\right)^n \tag{41}$$

$$\begin{aligned} A(N) &= \frac{N^N}{\Gamma(N)\mathrm{e}^N} \\ &\sim \frac{\mathrm{e}^{N-1}}{\sqrt{2\pi(N-1)}(N-1)^{N-1}}\frac{N^N}{\mathrm{e}^N} \\ &\sim \left(\frac{N}{N-1}\right)^{N-1}\frac{1}{\mathrm{e}}\frac{N}{\sqrt{2\pi(N-1)}} \\ &\sim \left(\frac{N}{N-1}\right)^{N-1}\frac{1}{\mathrm{e}}\sqrt{\frac{N}{2\pi}} \end{aligned} \tag{42}$$

By using the following identity:

$$\lim_{n\to+\infty}\left(\frac{n}{n-1}\right)^{n-1} = \mathrm{e} \tag{43}$$

we arrive at:

$$A(N) \sim \sqrt{\frac{N}{2\pi}} \tag{44}$$

It is important to note that $\lim_{N\to+\infty} A(N) = +\infty$.

Study of the $f(x, N)$ *function*

The $f(x, N)$ function has the following properties:

$$f(x, N) > 0 \quad \text{for all } x, N \geq 0 \tag{45}$$

$$f(0, N) = 0 \quad \text{for } N > 0 \tag{46}$$

$$\lim_{x\to+\infty} f(x, N) = 0 \tag{47}$$

$$f(x, N) \leq f(x_N, N) \quad \text{where } x_N = 1 - \tfrac{1}{N} \tag{48}$$

$$f(x_N, N) = \left(\frac{N-1}{N}\right)^{N-1}\mathrm{e} \to 1 \quad \text{when } N \to +\infty \tag{49}$$

$$f(x, N+1) \leq f(x, N) \tag{50}$$

It is also important to note that $f(x,N)$ is an increasing function from 0 to x_N and a decreasing function from x_N to $+\infty$.

Convergence of the $A(N)f(x,N)$ function

In order to prove that the $A(N)f(x,N)$ function converge to a Dirac function, we need to demonstrate the following properties:

$$\lim_{N\to+\infty}\int_{x=0}^{+\infty} A(N)f(x,N)dx = 1 \quad (51)$$

$$\lim_{N\to+\infty} A(N)f(x,N) = 0 \text{ for } x\neq 1 \quad (52)$$

$$\lim_{N\to+\infty} A(N)f(1,N) = +\infty \quad (53)$$

The property (51) is given by definition: $A(N)f(x,N)$ represents a probability density so for all N we have $\int_{x=0}^{+\infty} A(N)f(x,N)dx = 1$.

Proof of (53)**:** For $x=1$ we have:

$$\begin{aligned}\lim_{N\to+\infty} A(N)f(1,N) &= \lim_{N\to+\infty} A(N) \times \lim_{N\to+\infty} f(x_N,N)\\ &= \lim_{N\to+\infty} A(N)\\ &= +\infty \end{aligned} \quad (54)$$

Proof of (52)**:** For $x\neq 1$ we want to prove that $\lim_{N\to+\infty} A(N)f(x,N)=0$. In order to demonstrate this we need to proceed using *reductio ad absurdum*.

We suppose that there exists a $x_0\neq 1$, a $\xi>0$, a $N_0\geq 0$ such that for all $N\geq N_0$, $f(x_0,N)>\xi$. We suppose here that $x_0<1$. Note that the proof for $x_0>1$ is identical and is left to the reader. We can choose N_0 such that $N_0>\frac{1}{1-x_0}$. And note $\eta=\frac{1-x_0}{2}$.

$$\begin{aligned}\int_{x=0}^{+\infty} A(N)f(x,N)dx &\geq \int_{x=x_0}^{1-\frac{1}{N}} A(N)f(x,N)dx\\ &\geq A(N)\left(1-\frac{1}{N}-x_0\right)\\ &\quad \times \min_{x\in[x_0,1-\frac{1}{N}]}(f(x,N))\\ &\geq A(N).\eta.\xi \end{aligned} \quad (55)$$

So

$$\begin{aligned} A(N)\eta\xi &\leq 1 \\ \xi &\leq \frac{1}{\eta A(N)} \text{ for all } N > N_0 \end{aligned} \tag{56}$$

We deduce from the last equation that because $\lim_{N\to\infty} A(N) = +\infty$, $\xi = 0$ which is in contradiction with the hypothesis.

So for all $x \neq 1$, $\lim_{N\to\infty} A(N) f(x, N) = 0$ ■

ACKNOWLEDGMENT

This work was supported by the Engineering and Physical Sciences Research Council (EPSRC) Grant number EP/J015180/1 and the MOD University Defence Research Collaboration in Signal Processing Grant number EP/K014277/1.

REFERENCES

[1] H. D. Griffiths, C. J. Baker, P. F. Sammartino, and M. Rangaswamy, *MIMO as a Distributed Radar System*. John Wiley & Sons, Inc., 2008, ch. 8, pp. 319–363. [Online]. Available: http://dx.doi.org/10.1002/9780470391488.ch8

[2] J. Li and P. Stoica, "Mimo radar with colocated antennas," *Signal Processing Magazine, IEEE*, vol. 24, no. 5, pp. 106–114, Sept 2007.

[3] A. Haimovich, R. Blum, and L. Cimini, "MIMO radar with widely separated antennas," *Signal Processing Magazine, IEEE*, vol. 25, no. 1, pp. 116–129, 2008.

[4] D. Bliss and K. Forsythe, "Multiple-input multiple-output (MIMO) radar and imaging: Degrees of freedom and resolution," in *Proc. 37th Asilomar Conf. Signals, Systems and Computers*, 2003.

[5] E. Fishler, A. Haimovich, R. S. Blum, D. Chizhik, L. J. Cimini, and R. A. Valenzuela, "MIMO radar: An idea whose time has come," in *Proc. IEEE Int. Conf. Radar*, 2004.

[6] E. Fishler, A. Haimovich, R. Blum, J. Cimini, L.J., D. Chizhik, and R. Valenzuela, "Spatial diversity in radars-models and detection performance," *Signal Processing, IEEE Transactions on*, vol. 54, no. 3, pp. 823–838, March 2006.

[7] D. Rabideau, "Ubiquitous MIMO digital array radar," in *Proc. 37th Asilomar Conf. Signals, Systems, and Computers*, 2003.

[8] C. Du, "Performance evaluation and waveform design for MIMO radar," Ph.D. dissertation, Edinburgh University, 2010.

[9] N. Lehmann, E. Fishler, A. Haimovich, R. Blum, D. Chizhik, L. Cimini, and R. Valenzuela, "Evaluation of transmit diversity in MIMO-radar direction finding," *Signal Processing, IEEE Transactions on*, vol. 55, no. 5, pp. 2215–2225, May 2007.

[10] C. Du, Y. Petillot, and J. Thompson, "Predicted detection performance of MIMO radar," *Signal Processing Letters, IEEE*, vol. 15, pp. 83–86, 2008.

[11] F. Robey, S. Coutts, D. Weikle, J. McHarg, and K. Cuomo, "MIMO radar theory and experimental results," in *38th Asilomar Conference on Signals, Systems and Computers*, 2004.

[12] I. Bekkerman and J. Tabrikian, "Target detection and localization using MIMO radars and sonars," *EEE Trans. Signal Processing*, vol. 54, p. 3873?3883, 2006.

[13] N. Lehmann, A. Haimovich, R. Blum, and L. Cimini, "MIMO-radar application to moving target detection in homogenous clutter," in *Adaptive Sensor Array Processing Workshop at MIT Lincoln Laboratory*, 2006.

[14] ——, "High resolution capabilities of MIMO radar," in *Proc. 40th Asilomar Conf. Signals, Systems and Computers*, 2006.

[15] S. Kim, B. Ku, W. Hong, and H. Ko, "Performance comparison of target localization for active sonar systems," *Aerospace and Electronic Systems, IEEE Transactions on*, vol. 44, no. 4, pp. 1371–1380, 2008.

[16] M. Fewell and S. Ozols, "Simple detection-performance analysis of multistatic sonar for anti-submarine warfare," DSTO Defence Science and Technology Organisation, Tech. Rep., 2011.

[17] R. Been, S. Jespers, S. Coraluppi, C. Carthel, C. Strode, and A. Vermeij, "Multistatic sonar: a road to a maritime network enabled capability," in *UDT Europe, Undersea Defence Technology Europe, Naples, Italy*, 2007.

[18] F. Ehlers, "Final report on deployable multistatic sonar systems," NATO Undersea Research Centre, Tech. Rep., 2009.

[19] S. Benen and P. Berkel, "Fusion concepts for multistatic sonar systems," in *INFORMATIK 2011 - Informatik schafft Communities*, 2011.

[20] M. Daun and F. Ehlers, "Tracking algorithms for multistatic sonar systems," *EURASIP Journal on Advances in Signal Processing*, vol. 2010, 2010.

[21] D. Orlando and F. Ehlers, "Advances in multistatic sonar," in *Sonar Systems*. InTech, 2011, pp. 29–50.

[22] D. Grimmett, "Automatic identification of specular detections in multistatic sonar systems," in *OCEANS 2009, MTS/IEEE Biloxi - Marine Technology for Our Future: Global and Local Challenges*, 2009, pp. 1–10.

[23] G. J. Székely, M. L. Rizzo, and N. K. Bakirov, "Measuring and testing dependence by correlation of distances," *The Annals of Statistics*, vol. 35, pp. 2769–2794, 2007.

[24] M. Skolnik, *Introduction to Radar Systems*. Mc-Graw-Hill, 2002.

[25] C. Capus, Y. Pailhas, K. Brown, D. Lane, P. Moore, and D. Houser, "Bio-inspired wideband sonar signals based on observations of the bottlenose dolphin (tursiops truncatus)," *J. Acoust. Soc. Am.*, vol. 121(1), pp. 594–604, 2007.

[26] Y. Pailhas, C. Capus, K. Brown, and P. Moore, "Measured target responses to bio-inspired sonar pulses," in *Proceedings of the 8th European Conference on Underwater Acoustics, ECUA ?06*, 2006.

[27] R. Urick, *Principles of Underwater Sound*. McGraw-Hill, New York, 1975.

[28] Y. Pailhas, C. Capus, and K. Brown, "The multiview limitation of target classification by broadband echo analysis," in *IEEE Oceans 2007 Europe Conferences*, 2007.

[29] Y. Pailhas, C. Capus, K. Brown, and P. Moore, "Analysis and classification of broadband echoes using bio-inspired dolphin pulses," *J. Acoust. Soc. Am.*, vol. 127, no. 6, pp. 3809–3820, 2010. [Online]. Available: http://link.aip.org/link/?JAS/127/3809/1

[30] Y. Pailhas, C. Capus, and K. Brown, "Permanent scatterers detection using raw SAS data," in *European Conference on Underwater Acoustics, ECUA?12*, 2012.

[31] W. R. Hamilton, "Theory of systems of rays," *Transactions of the Royal Irish Academy*, vol. 15, pp. 69–174, 1828.

[32] R. Doolittle and H. Uberall, "Sound scattering by elastic cylindrical shells," *J. Acoust. Soc. Am.*, vol. 39(2), pp. 272–275, 1966.

[33] A. C. Berry, "The accuracy of the gaussian approximation to the sum of independent variates." *Trans. Amer. Math. Soc.*, vol. 49, pp. 122–136, 1941.

[34] D. J. Rabideau, "MIMO radar waveforms and cancellation ratio," *Aerospace and Electronic Systems, IEEE Transactions on*, vol. 48, no. 2, pp. 1167–1178, APRIL 2012.

[35] H. Khan and D. Edwards, "Doppler problems in orthogonal MIMO radars," in *Radar, 2006 IEEE Conference on*, April 2006, pp. 4 pp.–.

[36] G. V. K. Sharma and K. R. Rajeswari, "MIMO radar ambiguity optimization using phase coded pulse waveforms," *International Journal of Computer Applications*, vol. 61, no. 10, pp. 18–23, January 2013, full text available.

[37] X. Song, S. Zhou, and P. Willett, "Reducing the waveform cross correlation of MIMO radar with space time coding," *Signal Processing, IEEE Transactions on*, vol. 58, no. 8, pp. 4213–4224, Aug 2010.

[38] J. L. Rodgers and W. A. Nicewander, "Thirteen ways to look at the correlation coefficient," *The American Statistician*, vol. 42(1), p. 59?66, 1988.

[39] N.J.Willis, *Bistatic Radar*. Norwood, MA:ArtechHouse, 1991.

[40] A. Home and G. Yates, "Bistatic synthetic aperture radar," *IEEE RADAR 2002*, pp. 6–10, 2002.

[41] O. Arikan, "A tomographic formulation of bistatic synthetic aperture radar," in *Procedings of ComCon 88*, 1988.

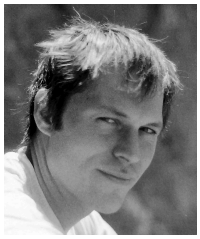

Yan Pailhas received the PhD degree in sonar systems and underwater acoustics from Heriot-Watt University, Edinburgh, UK in 2012 and the MSc. degree in signal and image processing from the Ecole Nationale Supérieure de Cachan, Cachan, France, in 2003. He also received two Engineering degrees in telecommunications with a specialization in image and signal processing from the Ecole Nationale Supérieure des Télécommunications, Paris, France, and from the Politecnico di Torino, Torino, Italy. He has been a Research Associate in the Ocean Systems Laboratory, Heriot-Watt University, Edinburgh, U.K., since 2004, where he is currently carrying out research activities in bioacoustic signals and sensors, signal processing for detection and classification, and numerical simulations.

Yvan R. Petillot (M03) received the engineering degree in telecommunications with a specialisation in image and signal processing, the MSc degree in optics and signal processing, and the PhD degree in real-time pattern recognition using optical processors from the Universitée de Bretagne Occidentale, Ecole Nationale Supérieure des Télécommunications de Bretagne (ENSTBr), Brest, France. He is a specialist in sonar data processing (including obstacle avoidance) and sensor fusion. He is currently a professor at Heriot-Watt University, Edinburgh, United Kingdom, where he leads the Sensor Processing Group of the Oceans Systems Laboratory, focusing on image interpretation and mine and counter measures. He is a reviewer of various IEEE Transactions and a member of the IEEE.

Keith Brown received the B.Sc. degree in electrical and electronic engineering in 1984 and his Ph.D. on the application of knowledge-based techniques to telecoms equipment fault diagnosis in 1988 from the University of Edinburgh, Edinburgh, Scotland. He is currently a senior lecturer at Heriot-Watt University and part of the Edinburgh Research Partnerships Joint Research Institute for Signal & Image Processing. His research interests in bio-inspired signal design and analysis and intelligent systems.

Prof. Mulgrew received his B.Sc. degree in 1979 from Queen's University Belfast. After graduation, he worked for 4 years as a Development Engineer in the Radar Systems Department at Ferranti, Edinburgh. From 1983-1986 he was a research associate in the Department of Electrical Engineering at the University of Edinburgh. He was appointed to lectureship in 1986, received his Ph.D. in 1987, promoted to senior lecturer in 1994 and became a reader in 1996. The University of Edinburgh appointed him to a Personal Chair in October 1999 (Professor of Signals and Systems). He currently holds the Royal Academy of Engineering Chair in Signal Processing . His research interests are in adaptive signal processing and estimation theory and in their application to radar and sensor systems. Prof. Mulgrew is a co-author of three books on signal processing.